# Halide Re-Shelled Quantum Dot Inks for Infrared Photovoltaics

James Z. Fan, Mengxia Liu, Oleksandr Voznyy, Bin Sun, Larissa Levina, Rafael Quintero-Bermudez, Min Liu, Olivier Ouellette, F. Pelayo García de Arquer, Sjoerd Hoogland, and Edward H. Sargent*

Department of Electrical and Computer Engineering, University of Toronto, 10 King's College Road, Toronto, Ontario M5S 3G4, Canada

Ⓢ *Supporting Information*

**ABSTRACT:** Colloidal quantum dots are promising materials for tandem solar cells that complement silicon and perovskites. These devices are fabricated from solution phase; however, existing methods for making infrared-bandgap CQD inks suffer agglomeration and fusion during solution exchange. Here we develop a ligand exchange that provides robust surface protection and thereby avoids aggregation. First, we exchanged long oleic acid ligands to a mixed system comprising medium-chain ammonium and anionic chloride ligands; we then reshelled the surface using short halides and pseudohalide ligands that enabled transfer to a polar solvent. Absorbance and photoluminescence measurements reveal the retention of exciton sharpness, whereas X-ray photoelectron spectroscopy indicates halide capping. The best power conversion efficiency of these devices is 0.76 power points after filtering through silicon, which is 1.9× higher than previous single-step solution-processed IR-CQD solar cells.
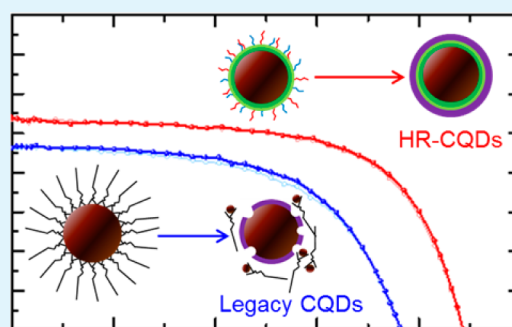
**KEYWORDS:** PbS quantum dot, infrared, photovoltaics, solution processed, ligand-exchange

Crystalline silicon (cSi) solar cells meet 90% of global demand for photovoltaics.[1] cSi photovoltaics offer power conversion efficiencies (PCEs) > 19% (module) and 25% (cell) and are stable for more than 25 years.[2] Thanks to continuous research and manufacturing advancements, the overall cost of cSi photovoltaic (PV) cells has decreased from 76 $/Wp in 1970 to less than 0.15 $/Wp in 2015.[3] As cSi approaches its ultimate performance limit, its rate of improvement has slowed correspondingly, with only a 3% increase in absolute PCE over a period of 15 years.[1,2,4] Recently, thin-film PV technologies, such as CuInGaS,Se (CIGS),[5] CdTe,[6] and hybrid organohalide perovskites[7] have all reached certified PCEs similar to that of cSi. However, all of these materials, including cSi, mainly rely on harvesting the visible portion of the solar spectrum, leaving much of the infrared portion unabsorbed.

Further improving the PCE of cSi full-spectrum harvesting solar cells requires new strategies, including multispectral/tandem approaches. The infrared wavelengths unabsorbed beyond silicon's 1100 nm bandgap represent one opportunity to add power points atop silicon's performance.[8]

Colloidal quantum dots (CQDs) are light-absorbing materials that can be developed into thin-film optoelectronic technologies such as lasers, light emitting diodes, photodetectors, and solar cells.[9−12] Their solution-processing and ambient stability enables the fabrication of large area, flexible solar cells.[13] Notably, the bandgap of CQDs can be readily tuned by changing their size,[8,14] making CQDs an option as back cells that augment wider-bandgap PV materials. Specifically, using PbS CQDs with an exciton peak positioned at wavelengths longer than cSi's absorption edge of 1100 nm

allows for efficient absorption of light in the IR.[8,14,15] Up to six absolute power points are available for addition to silicon in a four-terminal tandem cell.[8,14]

Recent advances in CQD materials engineering have led to CQD inks that enable a single-step deposition and record performance under the full AM1.5 solar spectrum,[16] offering advantages over place-exchange based devices[17] that include a smoother energy landscape in each of the conduction and valence bands. This process has been recently adapted for larger-bandgap CQDs as well.[14] Oleate capped CQDs in octane undergo a phase transfer to a polar solvent containing halide precursors and salts such as lead iodide and ammonium acetate. The dots are then concentrated into an ink for film deposition.[16] We denote these as legacy CQDs.

Unfortunately, this crucial first phase transfer step fails when it is applied to larger-size CQDs (4−5 nm).[18] The detachment of Pb(oleate)$_2$ species produces CQD aggregation and fusion.[19,20] In the resultant inhomogeneous energy landscape, carriers funnel to the lowest-energy bandtails, limiting quasi Fermi-level splitting and open-circuit voltage.[16] Macroscopically fused CQDs also make materials processing more difficult, leading to cracked and inhomogeneous films.[14] As a result, ink-based IR CQD PV cells have achieved a modest 0.4% silicon-filtered PCE.[14] Finding a way to utilize colloidal inks would
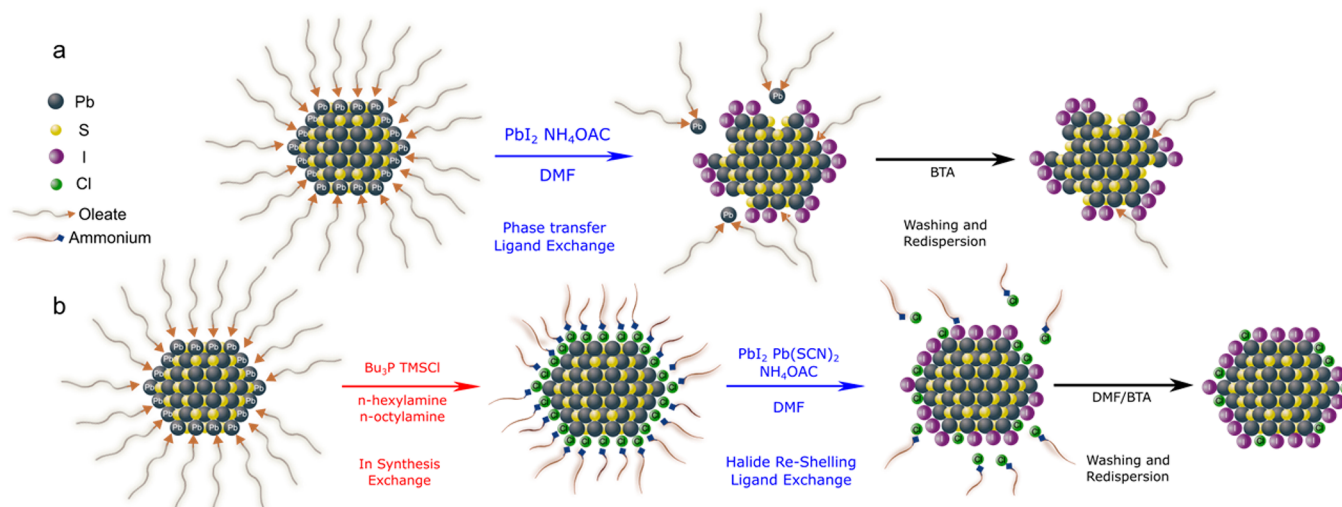
**Figure 1.** Visual representation of the ligand exchanges: (a) Legacy CQD exchange process for IR-CQDs. (b) Halide reshelling CQD exchange process for IR-CQDs.

reduce solvent waste, avoid multilayer deposition, and lead to more stable devices.

Here we engineer a new single-step ink deposition process to produce IR harvesting CQD devices to augment a standard cSi solar cell. We report herein a new two-stage ligand exchange process that preserves monodispersity and passivation in IR-CQDs. We show that the nanoparticles do not aggregate when dispersed in the desired polar phase from which films are processed. The photoluminescence quantum yield (PLQY) is 1.4× greater than in the legacy CQDs. X-ray photoelectron spectroscopy (XPS) reveals higher halide-to-sulfur ratios in the best films. The best performing devices made using this method produce 0.76 power points under silicon-filtered AM1.5 light. This is ∼2× higher than the best previously published solution-exchanged IR CQD device.

All synthetic strategies including device fabrication and testing are described in detail in the Supporting Information. Figure 1a shows the strategy to improve the colloidal stability of IR-CQDs (bandgap <1.1 eV, first exciton peak >1100 nm), comparing it to the legacy process.[14,19,21,22] Previous studies showed via 1H NMR a significant decrease in surface oleate after the PbS CQDs were treated with iodide species.[23] FTIR showed a significant decrease in $CH_x$ stretching signal and the disappearance of the C=O stretch after ligand[14,24] X-ray photoelectron spectroscopy revealed a lead to iodide ratio of 0.7, indicating that the surface is rich with atomic iodide ligands.[14,16] In the legacy process, the initially synthesized oleate-capped IR CQDs are dispersed in octane before undergoing a phase transfer to a polar solvent, N,N-Dimethylformamide (DMF), containing $PbI_2$ and ammonium acetate ($NH_4OAc$). It was previously suggested that PbS CQDs are capped with oleate and hydroxyl species passivating the (111) facets; and with physisorbed oleic acid on the (100) facets.[25] As the oleate-capped CQD enters the DMF phase and undergoes ligand exchange, surface oleic acid, oleate and Pb(oleate)$_2$ species are removed. During this process, the IR CQDs may undergo fusion and form nanosized and macroscopic (>1 μm) agglomerates. This occurs because as the CQD diameter is increased, the Pb-rich (111) surface is replaced by a more stable (100) surface.[26] The (111) facet is known to be ligand passivated while the (100) surface is generally self-passivated and more prone to fusion and oxidation. After this

phase transfer, the CQDs are precipitated and redispersed in butylamine (BTA) before film formation. Colloidal stabilization is achieved by ammonium ligands that form due to a reaction of BTA with moisture in air and trace amounts of $NH_4OAc$ remaining from the first step of ligand exchange in DMF.[16]

We redesigned this IR-CQD solution exchange by first incorporating a chloride passivation step (the in-synthesis exchange) and then a separate iodide passivation step (Figure 1b). Following the initial synthesis of oleate capped PbS CQDs, we injected tributylphosphine ($Bu_3P$) during the reaction cooling process to exchange with the oleic acid ligands.[19,21] Then the chloride source, trimethylchlorosilane (TMSCl), was injected into the reaction flask. The reaction vessel was then further cooled to allow the CQDs to precipitate. During this process, excess oleic acid and TMSCl formed HCl species in situ, which enabled the displacement of oleate species and promoted the formation of $[HPBu_3]^+[Cl]^-$ species on the PbS surface. The clear supernatant was discarded, leaving solid CQDs in the bottom of the flask. The intermediate ligands, a mixture of n-hexylamine and n-octylamine, were injected to redisperse the CQDs. This is possible because the amines displace the $PBu_3$ to form surface ammonium $[RNH_3]^+$ species that stabilize the CQDs.[19,21] The nanocrystals are therefore passivated with an adsorbed chloride and further charge stabilized by medium-chain ammonium ligands. This chloride passivation mechanism was studied in detail in the work by Anderson et al.[19,21] We denote these materials as the $[RNH_3]^+[Cl]^-$ CQDs.

Following the first stage of this ligand exchange, 50 mg of dried $[RNH_3]^+[Cl]^-$ CQDs was directly dissolved into 5 mL of a halide-rich DMF solution, containing 100 mM $PbI_2$, 10 mM $Pb(SCN)_2$, and 60 mM $NH_4OAC$ in ambient conditions. We denote this the iodide passivation step. The addition of the $Pb(SCN)_2$ species has been reported to reduce trap density compared to pure $PbI_2$ passivated CQDs.[27]

Density functional theory (DFT) suggests a mechanism by which the new exchange can avoid the loss of CQD passivation. In the new exchange, displacing the surface oleate ligand with the aid of TMSCl with the reaction PbS(oleate) + TMSCl → PbS(Cl) + TMS(oleate) is favorable by 0.2 eV. In comparison, in the legacy approach, directly starting with the iodine passivation reaction, PbS-Pb(oleate) + $PbI_2$ → PbS(I) +

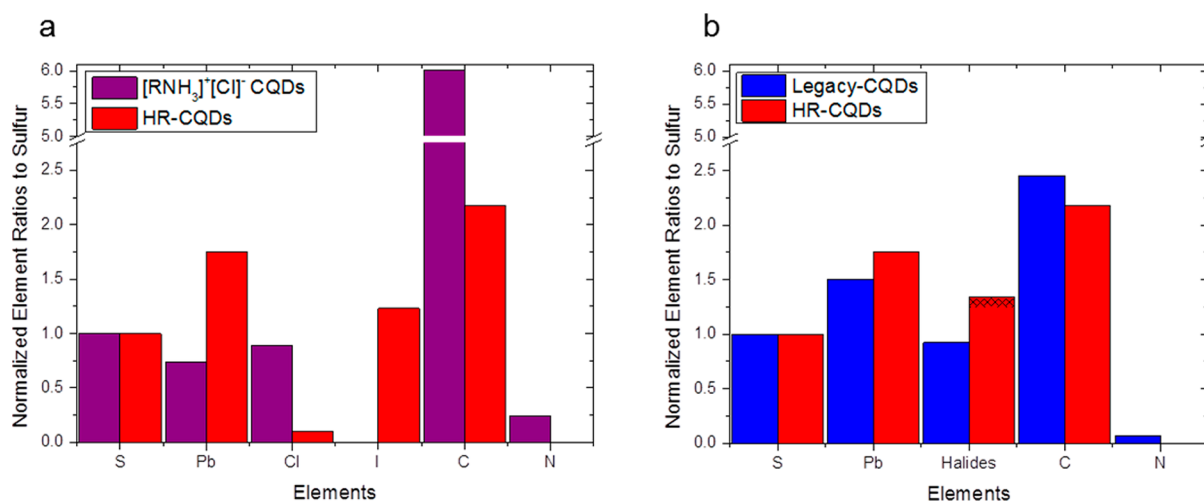**Figure 2.** XPS ratios. (a) Comparison between the as-synthesized $[RNH_3]^+[Cl]^-$ CQDs and fully processed HR-CQDs. (b) XPS comparison between legacy CQDs and HR-CQDs. The hatched area represents the additional chloride content.
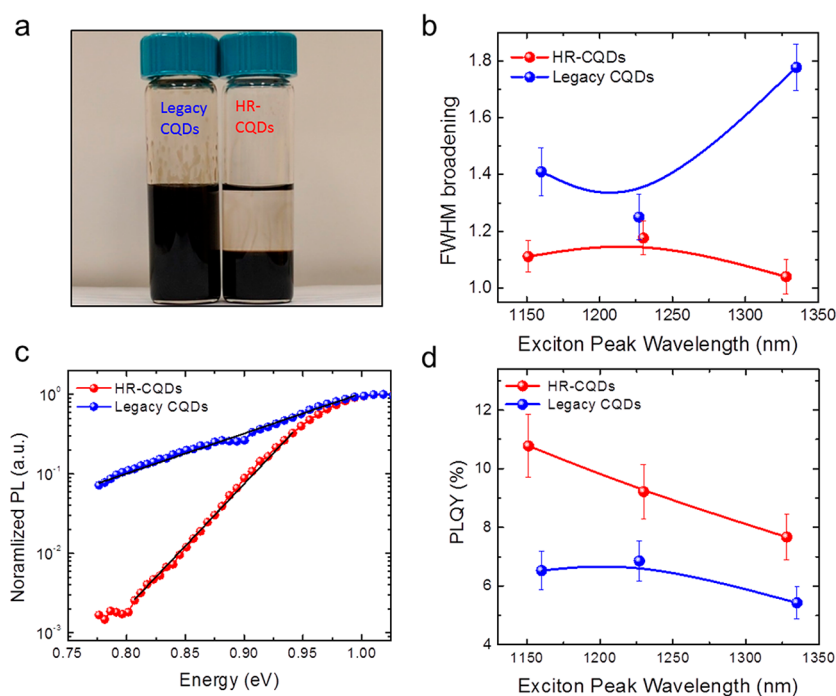


**Figure 3.** Visual and spectroscopic evidence revealing the difference the two ligand exchanges. (a) Vials reveal the effect of ligand exchange. The top layer in both vials is octane, whereas the bottom is the exchange solution in DMF. The legacy CQDs (left) cannot complete the phase transfer, whereas the HR-CQDs (right) is successfully transferred to the DMF. (b) Full width at half-maximum (fwhm) broadening comparing the two exchanges (broadening is defined as fwhm$_{as\text{-synthesized}}$/fwhm$_{fully\ processed}$). (c) Photoluminescence tail comparing the two processes for a 1 eV (∼1240 nm) CQD. (d) Photoluminescence quantum yield (PLQY) of the two exchanges. Lines in b−d are there to guide the eye.

PbI(oleate) is unfavorable by 0.13 eV. In the legacy approach, the direct detachment of Pb(oleate)$_2$ from the surface (0.74 eV) competes with the desired ligand exchange.[21] This results in the loss of surface protection and increases the chances for CQD aggregation and fusion.

To prepare devices, we need an additional halide reshelling step because the medium chain $[RNH_3]^+$ ligands end up in final films and decrease conductivity by spacing out the CQDs. XPS shows a high C:S ratio, which confirms the presence of $[RNH_3]^+$ ligands. Further, chloride-only passivated CQD films are not air-stable, as molecular O$_2$ may diffuse to the dot surface; this may lead to an increased density of midgap states.[28] XPS supports this view since we observe a higher O:S

ratio (Figure S1). Consequently, films directly spin-cast from this solution are also prone to macroscopic cracking and CQD fusing.[22]

We overcome these issues by displacing the ammonium ligands with halides and pseudohalides. The $[RNH_3]^+[Cl^-]$ CQDs disperse readily in a DMF solution containing PbI$_2$, NH$_4$OAc, and Pb(SCN)$_2$. These additional salts displace the ammonium cations and provide the necessary halide ions to reduce interdot spacing.[16,27] The addition of Pb(SCN)$_2$ reduced the overall trap density in the film. This was studied in detail by Sun et al.[27] Additional ammonium cations and adsorbed amines are removed during the washing process with hexanes. Finally, the CQDs were dispersed in a mixture of 10%
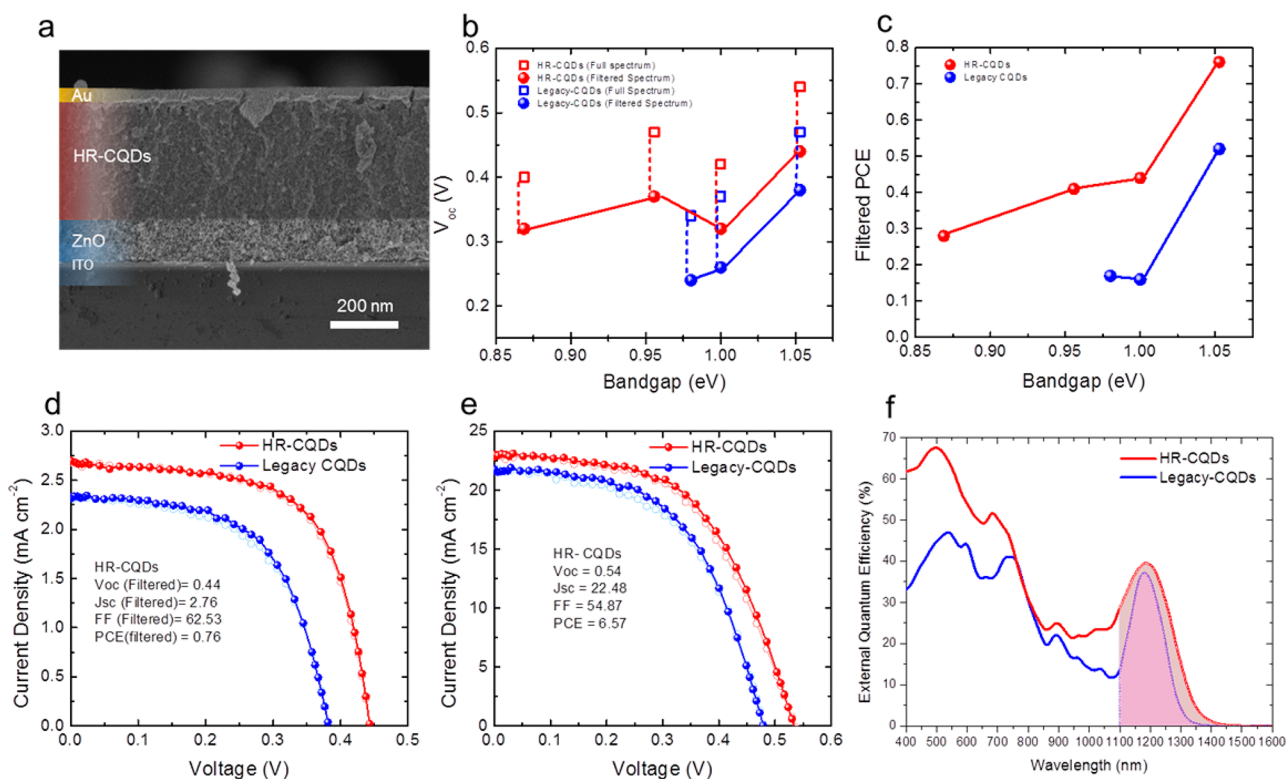
**Figure 4.** Solar cell device characteristics. (a) Cross-section scanning electron microscopy image of the hero HR-CQD device. (b) Full spectrum and cSi-filtered open circuit voltage comparison between legacy CQDs and HR-CQDs. (c) Filtered power conversion efficiencies comparison between legacy CQD and HR-CQD devices. (d) cSi-filtered hero $J-V$ characteristics comparison between legacy CQD and HR-CQD devices. (e) Full spectrum hero $J-V$ characteristics comparison between legacy-CQD and HR-CQD devices. Filled circles represent the forward scan while lighter circles represent the reverse scan for d and e. (f) External quantum efficiencies comparing the hero legacy-CQD and HR-CQD devices for the same wavelength.

V/V DMF to butylamine. The extra addition of DMF was used to stabilize these IR-CQDs.

The XPS elemental ratios (Figure 2a) reveal the importance of the second exchange stage. XPS evidence reveals a higher Pb:S ratio after room temperature halide treatment due to the additional Pb species that were added from the addition of $PbI_2$ and $Pb(SCN)_2$. We propose that the chloride ions act as a sacrificial shell during this process. Although the chloride content decreased after the iodide treatment, the total halide content has increased after the post treatment. This creates the possibility that more dangling surface bonds have been passivated using halides. Finally, the overall carbon content has decreased after the post-treatment, indicating that the inorganic halide ligands have successfully displaced the residual amine ligands. We term these final CQDs halide reshelled CQDs (HR-CQDs) because the addition of the second exchange step provides another halide shell that further passivates the QD core.

Additional XPS experiments were performed to compare HR-CQDs to the legacy CQDs. HR-CQDs have both higher lead content and higher total halide content (Figure 2b). A lower S:Pb ratio and higher S:C content for legacy-CQDs is consistent with the picture that the surface was stripped during the exchange process. The trace nitrogen seen only in the case of the legacy CQDs may be attributed to butylammonium stabilizing dangling bonds on the PbS surface. HR-CQDs, have very little nitrogen in the final film since the combined halides maintain charge balance on the PbS core. However, XPS is a weak technique to quantitate the amount of nitrogen; therefore

we performed Fourier transform infrared (FTIR) spectroscopy to characterize the presence of trace butylammonium in both films (Figure S3).

Spectroscopic and experimental observations of the exchange solution highlights the advantages of the HR-CQD passivation method for IR-CQDs. Visually, the legacy process applied to the large-diameter CQDs results in no clear phase separation between the nonpolar and polar phases (Figure 3a). Stirring or vortexing the CQDs leads to further CQD agglomeration and settling to the bottom of the reaction vessel.

The difference in absorption spectra before and after the full ligand exchanges also reveals the significant differences between the two processes. The broadening of the exciton peak before and after phase transfer is highlighted (Figure 3b, Figure S4). Broadening is defined as the ratio of the fwhm of as-synthesized CQDs to the fwhm of exchanged CQDs. For these IR-CQDs, the full width at half-maximum (fwhm) of the exciton peak widens dramatically following the legacy process. We observe this broadening due to light scattering from the macroscopically fused CQDs in the DMF solution.

HR-CQDs retain their exciton shape after the phase transfer to DMF. Visual observation (Figure 3a) and absorption analysis (Figure 3b, Figure S4) show that the phase transfer is complete and uniform. In addition, the calculated exciton peak-to-valley ratio for both DMF stabilized solubilized CQDs is higher for HR-CQDs as the size increases (Figure S5), showing well-preserved monodispersity after exchange. In contrast, legacy CQDs suffer a loss of passivation and monodispersity as the size gets larger.

The photoluminescence (PL) tail for the legacy CQDs is significantly broader than the HR-CQDs, as shown in the logarithmic plot (Figure 3d), reconfirming detrimental agglomeration. The broader tail indicates the more poly-dispersed system: additional carriers are funneled into the PL tail where they are likely to recombine in these aggregation-produced traps.[29] The PL tail is consistently broader for legacy CQDs for several sizes (Figure S6). In addition, a significant increase in PLQY for HR-CQDs implies fewer midgap recombination centers[23] in the HR-CQDs. These pieces of evidence suggest that the halide-reshelling of the CQDs is needed to produce a more ordered array of IR-CQDs, and this translates to better CQD devices.

To validate the improvements at a solar cell level, we fabricated PV devices using both HR-CQDs and legacy CQDs. The device architecture follows that of previously published results.[14,30] The cross-sectional scanning electron microscope (SEM) image in Figure 4a presents the structure of a complete device.

The solar cell device characteristics were measured under AM1.5G illumination at 100 mW/cm$^2$. To simulate the IR-device performance as a silicon-back cell, we placed an 1100 nm long-wave-pass filter in front of the AM1.5G lamp. A correction factor was used to account for the spectral mismatch between the solar simulator and the correct AM1.5G spectrum beyond 1100 nm.[8,14] The filtered open-circuit voltage ($V_{oc}$), short-circuit current density ($J_{sc}$), fill factor (FF), and PCE from the CQD devices represents the solar cell figures of merit that arise from additional absolute power points that can be added to a cSi device in a four-terminal tandem architecture.[15,31]

We compared the solar cell characteristics of legacy CQD devices and HR-CQD devices. For devices made from different sizes of IR-CQDs, it is evident that all HR-CQD-devices have much higher filtered $V_{oc}$'s than their legacy CQD counterparts (Figure 4b). This significant increase in $V_{oc}$ indicates that the new CQDs preserve their passivation better in the final device, contributing to consistently higher PCE (Figure 4c). The device external quantum efficiency (EQE) of the HR-CQDs is higher at all wavelengths for several different CQD sizes (Figure S7). The legacy CQD devices with 0.89 eV (~1400 nm) bandgap could not be processed at all: the film showed visible agglomerates and cracks, which lead to all pixels shorted on the device. The average filtered PCE for optimized devices over 11 samples is 0.53 ± 0.06%. Our highest performing IR-filtered PCE is 0.76 power points, which is 1.9× higher than that from the previously published report,[14] and 1.5× higher than our legacy-CQD control device (Figure 4c–e).

In conclusion, we designed a ligand exchange protocol that protects the surface of the IR-CQDs from fusing during the ligand exchange process. An in-synthesis exchange was used to introduce chlorine onto the surface, and a room-temperature exchange adds an additional final halide shell that results in the halide reshelled CQDs. Spectroscopic evidence shows that this new exchange is feasible for large IR-CQDS (>1100 nm) and PV devices fabricated by this method show a considerable increase in PCE when compared to the pervious exchange protocol. Further work will focus on designing CQD devices to harvest absorption in the 1770 nm region of the AM1.5 spectrum, which is the optimal region for fabricating an IR-CQD device.[8] We believe that further optimization of the HR-CQD method for CQDs of this size will bring us the promise of a cSi solar cell with a theoretically added 6 additional power points.

## ASSOCIATED CONTENT

### Supporting Information

The Supporting Information is available free of charge on the ACS Publications website at DOI: 10.1021/acsami.7b11449.

Experimental, XPS spectra (Figures S1 and S2 and Tables S1 and S2), FTIR (Figure S3), absorbance (Figure S4), peak-to-valley ratios (Figure S5), photoluminescence tailing (Figure S6), and EQE (Figure S7) (PDF)

## AUTHOR INFORMATION

### Corresponding Author
*E-mail: ted.sargent@utoronto.ca (E.H.S.).

### ORCID
James Z. Fan: 0000-0002-1594-865X
Mengxia Liu: 0000-0002-1676-705X
Oleksandr Voznyy: 0000-0002-8656-5074
Olivier Ouellette: 0000-0001-5708-5058

### Author Contributions
The manuscript was written through contributions of all authors. All authors have given approval to the final version of the manuscript.

## ABBREVIATIONS

cSi, crystalline silicon
PCE, power conversion efficiency
PV, photovoltaic
CIGS, CuInGaS,Se
CQD, colloidal quantum dots
PLQY, photoluminescence quantum yield
XPS, X-ray photoelectron spectroscopy
DMF, N,N-dimethylformamide
NH$_4$OAc, ammonium acetate
BTA, butylamine
Bu$_3$P, tributylphosphine
TMSCl, trimethylchlorosilane
DFT, density functional theory
HR-CQDs, halide reshelled colloidal quantum dots
Voc, open-circuit voltage
Jsc, short-circuit current density
FF, fill factor

## REFERENCES

(1) Jean, J.; Brown, P. R.; Jaffe, R. L.; Buonassisi, T.; Bulovic, V. Pathways for Solar Photovoltaics. *Energy Environ. Sci.* **2015**, *8* (4), 1200−1219.
(2) efficiency-chart.png (4350 × 2457) https://www.nrel.gov/pv/assets/images/efficiency-chart.png (accessed Mar 16, 2017).
(3) Farmer, J. D.; Lafond, F. How Predictable Is Technological Progress? *Res. Policy* **2016**, *45* (3), 647−665.
(4) Yoshikawa, K.; Kawasaki, H.; Yoshida, W.; Irie, T.; Konishi, K.; Nakano, K.; Uto, T.; Adachi, D.; Kanematsu, M.; Uzu, H.; Yamamoto,

K. Silicon Heterojunction Solar Cell with Interdigitated Back Contacts for a Photoconversion Efficiency over 26%. *Nat. Energy* **2017**, *2*, 17032.

(5) Ishizuka, S.; Yamada, A.; Matsubara, K.; Fons, P.; Sakurai, K.; Niki, S. Development of High-Efficiency Flexible Cu(In,Ga)Se 2 Solar Cells: A Study of Alkali Doping Effects on CIS, CIGS, and CGS Using Alkali-Silicate Glass Thin Layers. *Curr. Appl. Phys.* **2010**, *10*, S154−S156.

(6) First solar sets 18.7% record for CdTe solar cell efficiency. http://www.semiconductor-today.com/news_items/2013/FEB/FIRSTSOLAR_260213.html. 2013, (Accessed October 3, 2017).

(7) Saliba, M.; Matsui, T.; Seo, J.-Y.; Domanski, K.; Correa-Baena, J.-P.; Nazeeruddin, M. K.; Zakeeruddin, S. M.; Tress, W.; Abate, A.; Hagfeldt, A.; Grätzel, M. Cesium-Containing Triple Cation Perovskite Solar Cells: Improved Stability, Reproducibility and High Efficiency. *Energy Environ. Sci.* **2016**, *9* (6), 1989−1997.

(8) Ip, A. H.; Kiani, A.; Kramer, I. J.; Voznyy, O.; Movahed, H. F.; Levina, L.; Adachi, M. M.; Hoogland, S.; Sargent, E. H. Infrared Colloidal Quantum Dot Photovoltaics via Coupling Enhancement and Agglomeration Suppression. *ACS Nano* **2015**, *9* (9), 8833−8842.

(9) Konstantatos, G.; Howard, I.; Fischer, A.; Hoogland, S.; Clifford, J.; Klem, E.; Levina, L.; Sargent, E. H. Ultrasensitive Solution-Cast Quantum Dot Photodetectors. *Nature* **2006**, *442* (7099), 180−183.

(10) Lee, J.-S.; Kovalenko, M. V.; Huang, J.; Chung, D. S.; Talapin, D. V. Band-like Transport, High Electron Mobility and High Photoconductivity in All-Inorganic Nanocrystal Arrays. *Nat. Nanotechnol.* **2011**, *6* (6), 348−352.

(11) Dai, X.; Zhang, Z.; Jin, Y.; Niu, Y.; Cao, H.; Liang, X.; Chen, L.; Wang, J.; Peng, X. Solution-Processed, High-Performance Light-Emitting Diodes Based on Quantum Dots. *Nature* **2014**, *515*, 96.

(12) Fan, F.; Voznyy, O.; Sabatini, R. P.; Bicanic, K. T.; Adachi, M. M.; McBride, J. R.; Reid, K. R.; Park, Y.-S.; Li, X.; Jain, A.; Quintero-Bermudez, R.; Saravanapavanantham, M.; Liu, M.; Korkusinski, M.; Hawrylak, P.; Klimov, V. I.; Rosenthal, S. J.; Hoogland, S.; Sargent, E. H. Continuous-Wave Lasing in Colloidal Quantum Dot Solids Enabled by Facet-Selective Epitaxy. *Nature* **2017**, *544* (7648), 75−79.

(13) Kramer, I. J.; Moreno-Bautista, G.; Minor, J. C.; Kopilovic, D.; Sargent, E. H. Colloidal Quantum Dot Solar Cells on Curved and Flexible Substrates. *Appl. Phys. Lett.* **2014**, *105* (16), 163902.

(14) Kiani, A.; Sutherland, B. R.; Kim, Y.; Ouellette, O.; Levina, L.; Walters, G.; Dinh, C. T.; Liu, M.; Voznyy, O.; Lan, X.; Labelle, A. J.; Ip, A. H.; Proppe, A.; Ahmed, G. H.; Mohammed, O. F.; Hoogland, S.; Sargent, E. H. Single-Step Colloidal Quantum Dot Films for Infrared Solar Harvesting. *Appl. Phys. Lett.* **2016**, *109* (18), 183105.

(15) Ouellette, O.; Hossain, N.; Sutherland, B. R.; Kiani, A.; García de Arquer, F. P.; Tan, H.; Chaker, M.; Hoogland, S.; Sargent, E. H. Optical Resonance Engineering for Infrared Colloidal Quantum Dot Photovoltaics. *ACS Energy Lett.* **2016**, *1* (4), 852−857.

(16) Liu, M.; Voznyy, O.; Sabatini, R.; García de Arquer, F. P.; Munir, R.; Balawi, A. H.; Lan, X.; Fan, F.; Walters, G.; Kirmani, A. R.; Hoogland, S.; Laquai, F.; Amassian, A.; Sargent, E. H. Hybrid Organic−inorganic Inks Flatten the Energy Landscape in Colloidal Quantum Dot Solids. *Nat. Mater.* **2016**, *16*, 258−263.

(17) Zarghami, M. H.; Liu, Y.; Gibbs, M.; Gebremichael, E.; Webster, C.; Law, M. P-Type PbSe and PbS Quantum Dot Solids Prepared with Short-Chain Acids and Diacids. *ACS Nano* **2010**, *4* (4), 2475−2485.

(18) Choi, H.; Ko, J.; Kim, Y.; Jeong, S. Steric Hindrance Driven Shape Transition in PbS Quantum Dots: nderstanding Size-Dependent Stability Steric Hindrance Driven Shape Transition in PbS Quantum Dots: Understanding Size-Dependent Stability. *J. Am. Chem. Soc.* **2013**, *135*, 5278−5281.

(19) Anderson, N. C.; Owen, J. S. Soluble, Chloride-Terminated CdSe Nanocrystals: Ligand Exchange Monitored by 1H and 31P NMR Spectroscopy. *Chem. Mater.* **2013**, *25* (1), 69−76.

(20) Zherebetskyy, D.; Zhang, Y.; Salmeron, M.; Wang, L. W. Tolerance of Intrinsic Defects in PbS Quantum Dots. *J. Phys. Chem. Lett.* **2015**, *6* (23), 4711−4716.

(21) Anderson, N. C.; Hendricks, M. P.; Choi, J. J.; Owen, J. S. Ligand Exchange and the Stoichiometry of Metal Chalcogenide

Nanocrystals: Spectroscopic Observation of Facile Metal-Carboxylate Displacement and Binding. *J. Am. Chem. Soc.* **2013**, *135* (49), 18536−18548.

(22) Carey, G. H.; Levina, L.; Comin, R.; Voznyy, O.; Sargent, E. H. Record Charge Carrier Diffusion Length in Colloidal Quantum Dot Solids via Mutual Dot-To-Dot Surface Passivation. *Adv. Mater.* **2015**, *27* (21), 3325−3330.

(23) Lan, X.; Voznyy, O.; García De Arquer, F. P.; Liu, M.; Xu, J.; Proppe, A. H.; Walters, G.; Fan, F.; Tan, H.; Liu, M.; Yang, Z.; Hoogland, S.; Sargent, E. H. 10.6% Certified Colloidal Quantum Dot Solar Cells via Solvent-Polarity-Engineered Halide Passivation. *Nano Lett.* **2016**, *16* (7), 4630−4634.

(24) Ning, Z.; Dong, H.; Zhang, Q.; Voznyy, O.; Sargent, E. H. Solar Cells Based on Inks of N-Type Colloidal Quantum Dots. *ACS Nano* **2014**, *8* (10), 10321−10327.

(25) Zherebetskyy, D.; Scheele, M.; Zhang, Y.; Bronstein, N.; Thompson, C.; Britt, D.; Salmeron, M.; Alivisatos, P.; Wang, L.-W. Hydroxylation of the Surface of PbS Nanocrystals Passivated with Oleic Acid. *Science* **2014**, *344* (6190), 1380−1384.

(26) Choi, H.; Ko, J.-H.; Kim, Y.-H.; Jeong, S. Steric Hindrance Driven Shape Transition in PbS Quantum Dots: Understanding Size-Dependent Stability Steric Hindrance Driven Shape Transition in PbS Quantum Dots: Understanding Size-Dependent Stability. *J. Am. Chem. Soc.* **2013**, *135*, 5278−5281.

(27) Sun, B.; Voznyy, O.; Tan, H.; Stadler, P.; Liu, M.; Walters, G.; Proppe, A. H.; Liu, M.; Fan, J.; Zhuang, T.; Li, J.; Wei, M.; Xu, J.; Kim, Y.; Hoogland, S.; Sargent, E. H. Pseudohalide-Exchanged Quantum Dot Solids Achieve Record Quantum Efficiency in Infrared Photovoltaics. *Adv. Mater.* **2017**, *29*, 1700749.

(28) Ning, Z.; Voznyy, O.; Pan, J.; Hoogland, S.; Adinolfi, V.; Xu, J.; Li, M.; Kirmani, A. R.; Sun, J.-P.; Minor, J.; Kemp, K. W.; Dong, H.; Rollny, L.; Labelle, A.; Carey, G.; Sutherland, B.; Hill, I.; Amassian, A.; Liu, H.; Tang, J.; Bakr, O. M.; Sargent, E. H. Air-Stable N-Type Colloidal Quantum Dot Solids. *Nat. Mater.* **2014**, *13* (8), 822−828.

(29) Ravindran, T. R.; Arora, A. K.; Balamurugan, B.; Mehta, B. R. Inhomogeneous Broadening in the Photoluminescence Spectrum of CdS Nanoparticles. *Nanostruct. Mater.* **1999**, *11* (5), 603−609.

(30) Chuang, C.-H. M.; Brown, P. R.; Bulović, V.; Bawendi, M. G. Improved Performance and Stability in Quantum Dot Solar Cells through Band Alignment Engineering. *Nat. Mater.* **2014**, *13* (May), 796.

(31) Bailie, C. D.; Christoforo, M. G.; Mailoa, J. P.; Bowring, A. R.; Unger, E. L.; Nguyen, W. H.; Burschka, J.; Pellet, N.; Lee, J. Z.; Grätzel, M.; Noufi, R.; Buonassisi, T.; Salleo, A.; McGehee, M. D. Semi-Transparent Perovskite Solar Cells for Tandems with Silicon and CIGS. *Energy Environ. Sci.* **2015**, *8* (3), 956−963.